Coding versus collimation in pencil-beam X-ray diffraction tomography

Hazineh, Dean, Greenberg, Joel

Dean S. Hazineh, Joel A. Greenberg, "Coding versus collimation in pencil-beam X-ray diffraction tomography," Proc. SPIE 10999, Anomaly Detection and Imaging with X-Rays (ADIX) IV, 1099909 (14 May 2019); doi: 10.1117/12.2519469

Event: SPIE Defense + Commercial Sensing, 2019, Baltimore, Maryland, United States

Coding versus collimation in pencil-beam X-ray diffraction tomography

Dean S. Hazineh[a] and Joel A. Greenberg[a]

[a]Duke University, Dept. of Electrical and Computer Engineering, Durham, NC, USA

ABSTRACT

X-ray diffraction tomography (XRDT) is an exciting imaging modality because of its capacity to combine volumetric imaging with material discrimination. Despite this fact, practical implementation of such systems to security workflows have been fraught with challenges due to "real world" constraints–one of the most notable being a limitation on the total photon budget. This challenge is exacerbated given that one of the more pronounced trade-offs in XRDT system design is that between imaging performance and the quantity of relevant, scattered photons collected. Consequently, two approaches have emerged that operate at different ends of this trade-off continuum. At one extreme, direct tomography (DT) uses a high degree of collimation to realize robust resolution but suffers from low signal levels. At the other extreme, coded aperture XRDT (CA-XRDT) employs coded apertures which allow for detection of a substantially greater number of photons but at the cost of signal multiplexing and potentially less robustness to object extent. While these two systems differ only slightly in hardware (i.e. whether a collimator or coded aperture is used), a fair and fundamental comparison between the two is not straightforward and has never been performed. Furthermore, such an analysis is important for understanding the strengths and weaknesses of each system and thereby identifying an optimal architecture. In this paper, we first present our methodology to define the theoretical resolution of DT and CA-XRDT systems, focusing on the case of a pencil beam geometry. After using this approach to tweak system design in simulation such that both systems have the same theoretical average resolution, we then conduct a numerical investigation of the imaging performance of each system as a function of the measurement SNR and target object width for linear and area array detector geometries. We find in our particular simulation study that, while there are cases where both systems can identify and localize an object equally well, there are certain imaging scenarios where CA-XRDT outperforms DT and vice versa. In addition, we find that DT generally provides more information per photon than CA-XRDT but that there can be comparatively less information overall.

Keywords: X-ray Diffraction, Tomography, Direct Tomography, Collimation, Coded Aperture, Aviation Security

1. INTRODUCTION

X-ray diffraction tomography refers to an imaging method that provides spatially-resolved information about the molecular structure of a material by measuring the momentum transfer of scattered photons.[1] Although other penetrative, volumetric imaging methods exist and are deployable to the field of security, most notably X-ray computed tomography (CT),[2] XRDT has a notable advantage over transmission-based measurements in that the scattered photons are altered in a material specific way and can provide greater sensitivity for material identification. X-ray diffraction represents a gold standard in material analysis, and this fact alone makes the prospect of its use in tomography particularly attractive (even if implemented simply as an orthogonal or complimentary measurement); however, another feature unique to XRDT that encourages its further development is embedded in the fact that the X-ray diffraction approach naturally translates to an elegant, volumetric solution without the need of object rotation–the finite deflection of scattered X-rays lifts the degeneracy inherent in transmission tomography and makes snapshot (i.e. single measurement) scatter tomography architectures a reality.[3] While this imaging modality has been explored since the 1980's, the practical implementation of such systems to security workflows have been fraught with challenges imposed by "real world" constraints. As an

---

Further author information: (Send correspondence to J.A.G.)
J.A.G.: E-mail: jag27@duke.edu, Telephone: 1 919 660 0183

Anomaly Detection and Imaging with X-Rays (ADIX) IV, edited by Amit Ashok,
Joel A. Greenberg, Michael E. Gehm, Proceedings of SPIE Vol. 10999, 1099909
© 2019 SPIE · CCC code: 0277-786X/19/$18 · doi: 10.1117/12.2519469

example, in aviation security where baggage scanning benefits greatly from volumetric identification, a successful tomographic architecture should accommodate to an illumination time set by the belt speed, $\sim 0.2 - 0.5$ m/s, with little to no cool-down periods and should also have a X-ray source which operates off standard wall power. These two particular constraints together sharply limits the photon budget and exacerbates the challenge in scatter tomography of obtaining significant signal levels–a difficulty which stems from the fact that the scatter interaction strength is both small (corresponding to only a few percent of the incident photons) and diffuse (spread over a wide angular range).

While low signal levels may initially suggest the importance of collecting as many scattered photons as possible, the implementation is complicated due to the fact that current XRDT approaches operate with some trade-off between blocking portions of the scattered, measurable photons in exchange for improved system resolution and performance. Specifically, two potentially viable approaches for introducing XRDT to security workflows have emerged, operating at different ends of this trade-off continuum. At one extreme, direct tomography (DT) utilizes a high degree of collimation to realize robust resolution but at the cost of discarding the majority of measurable photons. At the other extreme, coded aperture XRDT (CA-XRDT) employs coded apertures to measure significantly greater amounts of the scatter signal but at the cost of increased multiplexing. Although these two systems may differ only slightly in hardware (i.e. whether a collimator or coded aperture is inserted in between the object and the detector), a fair and fundamental comparison between the two methods is not straightforward and has never been performed. While the trade-off continuum suggests that the strengths and weaknesses for each method are different, there are numerous choices in the design for each system that can potentially insert bias into a comparative study and shift favor from one to the other. As an example, in formulating the comparison, one must decide if the two systems should have the same hardware as one another or independently-optimized geometries, if the theoretical resolution of each system should be the same, or if the aforementioned "real world" constraints should be factored in as well. Despite the various choices that can be made for this comparative analysis, quantifying and understanding the strengths and weaknesses of each system is important to thereby identify an optimal XRDT architecture for various security applications.

In this paper, we present a comparative analysis of pencil beam DT and CA-XRDT systems, with effort being to understand how each system performs relative to signal strength (in the presence of Poisson noise) and object width/complexity. Here, we choose to conduct an unbiased study in the sense that both systems are designed to have the same theoretical, spatial and momentum transfer resolution so that differences in imaging performance may be attributed to the tomographic architecture itself rather than resulting from differences introduced in our system design. Furthermore, by comparing systems of matched theoretic resolution, we can better understand how each system depends on and makes use of the total available photon budget. In this work, we will first present a more in depth review of CA-XRDT and DT systems, as it is useful in order to understand the options for the system design, and in doing so, we will also review and present analytic relations for system resolution. We will then present a numerical approach to define the average resolutions for each architecture based on a discretized, numerical model for each system and compare the results to theory. After ensuring that the resolutions are matched, we then conduct a numerical investigation of the imaging and classification performance using our XRDT simulation tool and discuss our findings.

2. DT AND CA-XRDT ARCHITECTURE THEORY

2.1 Basics of X-ray diffraction imaging

As XRDT is based on the principles governing X-ray diffraction, it is worthwhile to first note the basic physics at play for mapping measurements of coherently scattered photons to information about a material's molecular structure. The relevant elastic scattering process is known as Rayleigh scattering and occurs for all atoms that are illuminated by the X-ray beam. For atoms located within a coherence volume, the scattered fields have a well-defined phase relationship (dependent on the atomic arrangement) and can therefore interfere with each other to produce angular and spectral structure in the scattered distribution. This process can be summarized by describing the probability for an X-ray of energy E to undergo coherent scatter into a solid angle $d\Omega$ via the differential scatter cross-section, defined as

$$\frac{d\sigma_{coh}(E)}{d\Omega} = \frac{r_e^2}{2}\left[1+\cos^2(\theta)\right] f(q). \tag{1}$$

Here, r_e is the classical electron radius, θ is the X-ray deflection angle relative to the incident beam, and $f(q)$ is the squared molecular interference function, which we will simply refer to as the form factor throughout. Again, the form factor combines chemical and structural information, and it is the quantity that one seeks to image on a per voxel basis in XRDT. If an object is small and if its location relative to the source-detector geometry is known, one can then determine the form factor by making measurements of the scatter distribution and converting to the momentum transfer, q, basis through use of Bragg's law, which can be given in scalar form as,

$$q \equiv \frac{E}{hc}\sin\left(\frac{\theta}{2}\right), \tag{2}$$

with h and c representing Plank's constant and the speed of light, respectively. Specifically, Equation 2 reveals that there are in fact two, distinct types of measurements that can be made in order to determine the scatter intensity at each value of q when the object's location relative to the detection geometry is known. The deflection angle θ can be fixed and the form factor can be obtained by a spectroscopic measurement and a polychromatic source, as is done in energy-dispersive X-ray diffraction imaging, or alternatively, the energy of the photons can be fixed (or measured upon detection) and the form factor can be obtained by analyzing the distribution across θ, as is done in angle-dispersive X-ray diffraction imaging. While there are subtleties relating to the orientation of the lattice grating vector that results in additional requirements for defining the form factor of highly-crystalline materials,[1,4] the above can be generally sufficient for identification of most common objects. These two X-ray diffraction approaches serve as the foundations for the collimation– and coded aperture– based tomographic architectures reviewed here, respectively.

Alternatively, one can consider the case of when the object's location is no longer known, as is true when one is imaging a concealed or inherently volumetric object. Specifically, it is instructive if we utilize the pencil beam imaging scenario as an example and redefine the deflection angle as $\theta = \text{atan}(r/\text{d}z)$, where r is the radial distance from the pencil beam traveled by the scattered photon upon arrival at a detection plane and dz is the axial distance between the origin of scatter and the detector. Utilizing this definition with Equation 2, we now observe that, even with a simultaneous measurement of both a scattered photon's energy and its location at the detector, the momentum transfer value associated with the detection of the single photon is still undefined. Specifically, there now exists a $q-dz$ ambiguity which must be broken in XRDT, and in the following subsection, we will review how this is resolved utilizing collimators and coded apertures.

2.2 DT and CA-XRDT methods and resolution

In Figure 1A., a schematic display of a pencil-beam DT system is shown where scatter originates from multiple points along the length of the beam. To avoid multiplexing at the detector, a collimator with a fixed angle relative to the primary beam is utilized in order to limit the detector field of view and to create a direct mapping between each object voxel and detector pixel. This mapping is the key to resolving the aforementioned $q-dz$ ambiguity, and all photons scattered into angles outside the angular field of view are attenuated and not used. For each individual pixel to record the scatter intensity for all q values within a range of interest, each detector pixel must be energy sensitive and the primary beam must be polychromatic. In the image shown, illumination is explicitly drawn for a single column of detector pixels, which is in fact sufficient to image all object voxels along the length of the pencil beam; however, one can introduce redundancy in the measurement by utilizing the full scatter ring and designing the detector-side collimator such that a ring of detector pixels image each voxel. Although not necessarily viable for fan or cone-beam illumination scenarios, this method can improve the signal-to-noise ratio (SNR) if a 2D energy-sensitive detector is available. One useful aspect of DT to note is that the scatter signal is directly related to the form factor and is therefore interpretable without need for computational reconstruction (although such algorithms can enhance and improve q resolution, as is shown later in this work). On the other hand, DT faces two potential challenges which in fact commensurate with one another and

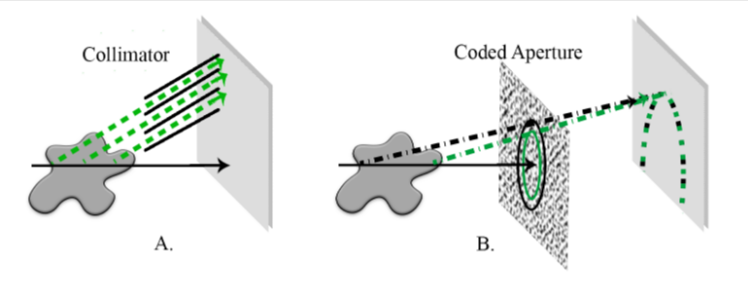

Figure 1. Schematic for various XRDT techniques in a pencil-beam X-ray system: A) DT in which a collimator is used and B) CA-XRDT in which a coded aperture is used. Here, the solid black line with an arrow indicates the primary beam, the dashed lines with an arrow indicate the scattered X-rays, and the gray square represents the detector.

echo the fundamental tradeoff in XRDT noted before: good spatial and momentum transfer resolution in this architecture requires extremely narrow angular collimation at the detector (which, for one, can be difficult to manufacture), but this need to block the majority of scattered X-rays in order to obtain well-conditioned signals furthermore results in extreme photon starvation and a poor signal to noise ratio.[5,6]

To obtain a reasonable approximation for the spatial resolution, Δz, achievable in a DT system, one can assert that the object voxel widths are defined entirely by the collimator angle, θ, and the angular field of view, ± dθ. Here, we have assumed a perfect pencil beam of negligible width and no angular extent. By projecting the line of sight from the detector pixels to the primary beam axis, the resolution along the beam, which we here define as being along the z axis, can be written as

$$\Delta z(z) = (z_d - z_o)\tan(\theta)\frac{\tan(\theta + d\theta) - \tan(\theta - d\theta)}{\tan(\theta - d\theta)\tan(\theta + d\theta)}, \tag{3}$$

where z_d and z_o is the location of the detector and the object voxel, respectively. The scaling in this relation is dominated by the fact that the field of view for each detector pixel translates to a larger voxel length as the separation distance between the object voxel and detector increases. We also note that this analytic relation has assumed that the field of view for detector pixels do not overlap with each other, which is in fact generally not true and can result in a better resolution than that predicted here. To compute an approximation for the momentum transfer resolution, we propagate the uncertainty in Bragg's law (Equation 2), resulting in a variance relation given as

$$\Delta q(q, E) = q\sqrt{\left(\frac{\Delta\theta}{\theta}\right)^2 + \left(\frac{\Delta E}{E}\right)^2}. \tag{4}$$

Here, the uncertainty in angle $\Delta\theta$ is twice the angular field of view, $d\theta$. The energy resolution ΔE is a property of the detector, and we choose to define it via the full width at half maximum (FHWM) of a representative Gaussian blurring kernel.

In Figure 1B., a schematic similar to the DT configuration diagram is shown but here illustrating the CA-XRDT approach; a pencil beam illuminates an object but, in place of a collimator, one instead employs a coded aperture.[7] While the two optical elements are similar in that they attenuate the X-ray signal at the aperture plane, a coded aperture is different in that it allows the transmission of X-rays at all angles. As a result, scatter from a broad range of locations can be visible to the detector at the same time and at the same pixel locations. This structured scatter approach results in a bright, multiplexed signal at the detector and in order to back out the spatially localized form factors, post-processing is necessary. The key insight required to demultiplex this signal lies in the fact that, if done correctly, each object voxel along the path of the beam projects a unique shadow of the coded aperture onto the detector by virtue of the position dependent magnification (and/or parallax in the fan or cone-beam illumination scenarios). In varying the properties of the coded aperture, one can then control the degree of multiplexing and relatedly, the imaging performance of the system.

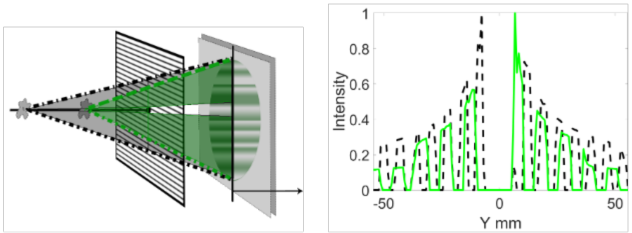

Figure 2. Schematic of a CA-XRDT system in which two scatterers located at different axial locations give rise to signals that overlap at the detector but are modulated with different code magnifications (i.e., spatial frequencies). The lineplot shows an example measurement along one column of pixels on the detector.[1]

The role of this detection-side coded aperture in breaking the tomographic $q - dz$ ambiguity is further illustrated in Figure 2, where we display representative data for a measurement of a cone of scatter at the detector created by the superposition of scatter from two different voxels along the pencil beam. Although the scatter overlaps at the detection plane, each set of overlapping rays intersects the coded aperture plane at different locations and thus obtains distinct modulations. In the corresponding line-plot in the figure, a single line/column of the detector measurement for the scatter originating from each object voxel alone is displayed and color coded. An actual experimental measurement would be the superposition of the intensities of both lines, and given that the modulations are unique for each object voxel, the superposition is itself unique. As a note, we emphasize that this uniqueness and perfect invertibility of the superposed signal is far easier with two dimensions of coded data versus one since more modulations can be applied to the full Debye ring. Furthermore, this also suggests that the smaller the ring, the fewer the number of modulations that can be encoded and thus the system's conditioning for inversion is worsened. Lastly, we highlight that the CA-XRDT approach explicitly assumes that the scatter signal is spatially or spectrally distributed (the former is the more conventional scenario), and consequently, the modulations must be appropriately coded in the spatial or spectral dimension, respectively.[8] For our particular implementation, we use the method based on the angle-dispersive X-ray diffraction approach and thus code spatially, but since we consider detectors that have an energy resolution capability, we also incorporate data from multiple energy channels to provide additional measurement diversity. Lastly, we emphasize that while the spatial resolution in DT is dependent on blocking a majority of the scatter signal, CA-XRDT generally enables the measurement of at least one order of magnitude more signal (while achieving the same theoretical resolution) at the cost of increasing multiplexing and post-processing complexity.

A reasonable analytic approximation for the spatial resolution achievable in a CA-XRDT system can be found in literature[3,9] and can be rewritten as,

$$\Delta z(z, q, E) = \frac{L_f (z_d - z_o)^2}{L_d (z_d - z_m)}, \tag{5}$$

where z_m is the location of the coded aperture along z, L_f is the feature size in the coded aperture, and L_d is the effective illumination length at the detector onto which coded modulations can be measured. Although useful as an approximation, correctly applying this relation to the description of physical systems is challenging since there is ambiguity in the true ratio of L_f/L_d, especially for a multi-energy architecture. Specifically, the value of L_d for a given object voxel is dependent on the relevant range of values in both q and E, and furthermore, not all energy channels are equally informative. Due to both the energy-dependent cross-section of scattering and the tube spectrum from which the X-rays originate from, the resolution may be dominated by only a small subset of energy channels, subsequently resulting in a smaller value of L_d than one may naively first assume. To define our own approximation to the momentum transfer resolution, we again use the variation relation in Equation 4 and define $\Delta\theta$ as

$$\Delta\theta(z,q,E) = \sin^{-1}\left(\frac{L\cos^2(\theta)}{z_d - z_o}\right), \tag{6}$$

where L is the larger value between the detector pixel size or the coded aperture feature size. This definition has been obtained by asserting that the larger length corresponds to a minimum angular resolution about a ray traveling from a point along the pencil beam to a point on the detector.

3. STUDY DESIGN

3.1 Matched resolution system design

Given an understanding of how to design a CA-XRDT or DT system and which parameters are relevant to the performance in each, we next consider what values to set for these parameters and how that alters the conclusions to be drawn from this study. We highlight that there are numerous constraints to a realistic X-ray tomographic system as applied to the security setting, and one could consequently define systems for comparison in a few different ways. Notably, it is important to understand which of the two systems can provide the highest fidelity estimates for an imaged object given a fixed budget for the design or given a limited, predefined set of hardware (i.e. detector and sources) or even given the freedom to make the most optimized and state-of-the-art build that is possible for each architecture. However, while these are useful, task-specific trade studies necessary for transitioning the technology to a particular industrial application, a comparison of CA-XRDT and DT systems based on this method alone would indicate the superior system for a particular scenario but would likely prove difficult to extrapolate from when the task or constraints change again. Instead, we are interested in understanding how CA-XRDT and DT systems with matched image quality in the infinite SNR limit (and for simple objects) compare to each other across a range of imaging scenarios by virtue of the fundamental way in which they make use of the scattered signal. While there may be overlap in their performance, we seek to probe if there exists imaging conditions for which one or the other fundamentally outperforms and is better conditioned for.

Specifically, given that the XRDT approaches reside at different extremes in the trade-off space, we anticipate that DT is an ideal implementation for localizing and identifying objects in the limit of infinite SNR; however, its breakdown in the low SNR limit is well known.[6] Regardless of the system design, a minimum number of detected photons is required to fill out the shape of the form factor, and given that CA-XRDT architectures can obtain orders of magnitude more photons when placed in the same detection geometry, we suspect that there are conditions in which a DT system fails while the CA-XRDT system succeeds. In analyzing imaging performance while tuning SNR and object width, we would like to be able to associate, as best as possible, the differences in performance to fundamental differences in the architecture, as opposed to artifacts stemming from the resolution of each system. We therefore choose to conduct this study in the context of matched resolutions. In this work, we model CA-XRDT and DT systems with parameters tuned such that the average spatial and momentum transfer resolutions are the same throughout the imaging volume. While we have presented and derived analytic relations for the theoretical spatial and momentum transfer resolutions of CA-XRDT and DT systems in Section 2.2, we have not yet presented validation or further support for their predictions. Instead, we highlight that our numerical, ray-tracing simulation tool for XRDT presents an alternate method to define the resolution of each system via use of the Gramian matrix. As our simulation tool has been validated in past works[10,11] and will serve to generate approximations to the tomographic measurements needed for our comparitive analysis, we will base our resolution comparison on this method predominantly and will utilize the theoretic relations primarily for system design guidance and as an important check that the resolutions obtained via this method are consistent with expectations from theory. In the remainder of this section, we first present a brief review of our simulation tool for X-ray diffraction and expand on how the Gramian matrix is calculated using the model. Following, we will discuss our approach to defining and obtaining resolution from this method and lastly, we will then present the average resolution for an exemplary matched configuration used in this study.

3.2 XRDT numerical simulation

More thorough details of our simulation approach can be found in a previously published work;[3] however, we summarize noting that the process relevant to this analysis begins by discretizing 3D space and defining a set of points to represent the full range of potential object locations. The impulse response from each of these points individually will be computed in order to obtain numerical predictions of the scatter, and for this reason, it is important to sample the simulated object space finer than the targeted/anticipated resolutions of the system. Here, we utilize the theoretic relations previously outlined for guidance in the pencil beam tomography scenario and define a set of scattering centers along a line with 2.5 mm spacing to represent a discretized version of the object. In addition, we compute the scatter for momentum transfer values between 0.05 and 0.35 $1/\mathring{A}$ with a step size of 0.002 $1/\mathring{A}$. These choices are consistent with the target average spatial and momentum transfer resolutions that characterize the systems modeled in this work, which are $\approx$ 10 to 20 mm and $\approx$ 0.006 to 0.010 $1/\mathring{A}$, respectively. We highlight that attenuation along the primary beam is included in our calculation, where we use the attenuation properties of water as representative for the materials considered. We justify this approximation given that our final results are averaged across a wide range of materials. In addition, we assert the small-angle approximation for scatter where the attenuation along the deflected path is assumed to be equal to that along the primary beam.

We define the energy spectrum of the pencil-beam incident on the object as that generated from a Tungsten filament with 0.5 mm of Aluminum filtration and 160 kV tube potential. The shape of this spectrum is obtained from numerical simulation via the published tool, SpekCalc,[12,13] which has been previously validated against Monte Carlo predictions.[14] Furthermore, the precise scaling of this curve is equally important in this work since we are interested in predicting the correct number of photons that reach the detector as a function of mAs; in Section 4.1, we present a discussion on an experimental based approach taken to determine the correct scaling. Next, we define a discrete, virtual detector consisting of either a 1D or 2D array of pixels with energy resolution. Specifically, our detector has contiguous, square pixels 0.75 mm in length and is modeled by a grid of points sub-sampled at 0.15 mm spacing and binned to create the macroscopic pixel–the rebinning process is necessary in order to get results that match well with experiment and better mimic a continuous, physical detector. In order to obtain a realistic energy response for these simulated pixels, we blur the incident photon energy spectrum with a Gaussian function defined by a FWHM = 2 KeV. We then consider energies for detected photons between 17.33 and 127.33 KeV, sampled in energy bin steps of 1 KeV. This energy set is chosen so that the form factors in the direct tomography system are sampled in q at approximately 0.002 $1/\mathring{A}$ across the range of interest. Lastly, we note that optical components such as collimators and coded apertures are virtually defined and included in the simulation.

With the tomographic geometry defined, we then compute the detector measurement by evaluating the number of photons scattered along each ray connecting a point in the object set to a point on the detector. Here, we define this path as $\vec{r}_{od}$, where each ray is evaluated for all q and E combinations to determine the measurement $\mathbf{g}$ according to

$$\mathbf{g}(q, E, \vec{r}_{od}) = \int dq \Phi(E) \frac{d\sigma_{coh}(E)}{d\Omega} \Delta\Omega T(E, \vec{r}_{od}) \delta(E'). \tag{7}$$

Here, $\Phi(E)$ is the pencil beam energy spectrum, $d\sigma_{coh}(E)/d\Omega$ is the differential coherent scatter-cross section given in Equation 1, $\Delta\Omega$ is the differential solid angle subtended by the detector pixel, and $T(E, \vec{r}_{od})$ is a transmission function that incorporates the aforementioned attenuation effects and also models the coded aperture or collimator component. The delta function, $\delta(E')$, enforces the E-q condition for Bragg's law, where $E' = E - hcq/\sin(\theta/2)$. While Compton scattering can be included by substituting in the total scatter cross-section in place of σ_{coh}, in this work we only model coherent scatter. Additionally, we note that this approach does not currently include multiple scattering, and while higher order scatter can be better included by utilizing a Monte Carlo approximation, this numerical ray-tracing approach is advantageous for this study since it allows for rapid simulation of many object scenarios. To highlight this fact, one can consider that all discrete, relevant rays are determined once the simulation geometry/space is fully defined; furthermore, Equation 7 reveals that the number of photons scattered along a particular ray only has an object dependence via a scaling with $f(q)$.

These facts allow us to pull out the object dependence from the calculation and define the approximated detector measurement $\mathbf{g}$ via,

$$\mathbf{g} = \mathbf{H}\mathbf{f} = \begin{bmatrix} g(z_1, q_1, E_1, xy_1) & g(z_1, q_2, E_1, xy_1) & \dots & g(z_m, q_n, E_1, xy_1) \\ g(z_1, q_1, E_1, xy_2) & g(z_1, q_2, E_1, xy_2) & \dots & g(z_m, q_n, E_1, xy_2) \\ \vdots & \vdots & \ddots & \vdots \\ g(z_1, q_1, E_k, xy_l) & g(z_1, q_2, E_k, xy_l) & \dots & g(z_m, q_n, E_k, xy_l) \end{bmatrix} \begin{bmatrix} f(z_1, q_1) \\ \vdots \\ f(z_1, q_n) \\ \vdots \\ f(z_m, q_1) \\ \vdots \\ f(z_m, q_n) \end{bmatrix}. \tag{8}$$

Here, we refer to $\mathbf{H}$ as the forward matrix, and it contains the object-independent projection coefficients extracted from Equation 7. Specifically, we he have denoted each of the matrix values as $g(z, q, E, xy)$, which represents the value of the projection coefficient mapping a scattered photon of energy E from a particular z voxel and q value to a particular x and y pixel location at the detector (referred to here via the notation xy). We refer to the vector $\mathbf{f}$ as the object vector, and its components represent the intensity of the form factor at the particular z location and q value. To summarize, the forward matrix describes the detector impulse response resulting from scatter originating at each z location within the object space, and the final image is obtained by matrix multiplication with the object vector, which contains information about the location of the object in our simulated space and the form factor associated to those voxels. Lastly, we highlight that a noise model is here included by introducing Poisson noise directly to the detector image $\mathbf{g}$.

3.3 Gramian resolution analysis

Building on the simulation framework outlined in the previous subsection, we now review our model-based method to obtain predictions for the $z-$ and $q-$dependent spatial and momentum transfer resolutions in DT and CA-XRDT systems, as is necessary for the matched-resolution study. First, we bring attention to the fact that in generating the detector measurement via the matrix multiplication of $\mathbf{H}$ and $\mathbf{f}$, each column of the forward matrix is scaled by a single z, q pair value. Specifically, each column in the forward matrix encodes the impulse response to that pair, independent of all others, and this principle serves as the basis of our resolution analysis. In order to both determine the form factor and localize the scattering origin from a snapshot XRD measurement, each impulse response should be maximally orthogonal and thus uniquely distinguishable. We can consider the cosine of the angle between the impulse responses as a similarity metric and numerically characterize how well-conditioned the geometric forward projection is for this type of tomographic inversion. Here, we do so via computing the normalized Gramian matrix G, whose elements are defined as

$$G_{i,j} = \frac{\langle \mathbf{H}_i, \mathbf{H}_j \rangle}{\|\mathbf{H}_i\| \cdot \|\mathbf{H}_j\|}, \tag{9}$$

where the subscript on $\mathbf{H}$ enumerates a particular column within the larger forward matrix and the operation in the numerator is the standard vector inner product.

In Figure 3A., we display, as an example, the full Gramian matrix obtained from the forward matrix describing our DT system. Although sparse, the Gramian resembles the identity matrix and has off-diagonal elements with intensities that rapidly falls off moving away from the main diagonal. In order to extract resolution values from the Gramian, we first take a row from the matrix (as exemplified via the horizontal red line in the image) and reshape it into a new matrix according to the known dimensions of the object space, as shown in image B. Specifically, each row in our Gramian contains the cosine of the angle between the detector measurement for a particular z, q impulse and the detector measurement for all other impulse pairs, and we can restructure the vector in order to observe the similarity in the $z - q$ space. From there, we define the resolution for the z, q pair corresponding to the row isolated in image A. by taking the lines of data at fixed z and q through the known object position (resulting in plots C. and D.) and calculating the FWHM of the two curves. This process is then

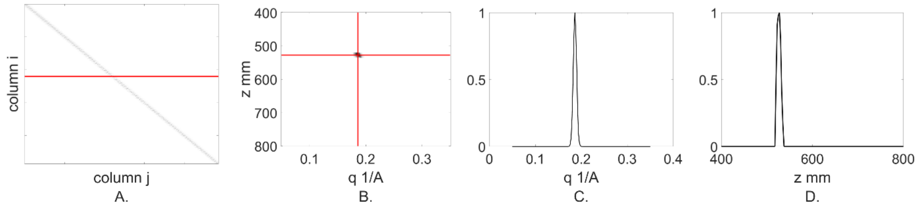

Figure 3. Outline of the Gramian approach to define system resolution: A) The Gramian for the 1D DT sytem used in this work is shown and in B) the single row highlighted in the Gramian matrix is reshaped to show the orthogonality between a z, q impulse and surrounding impulses. In C), the slice through z is plotted to then obtain the FWHM and in D), the slice through q is shown.

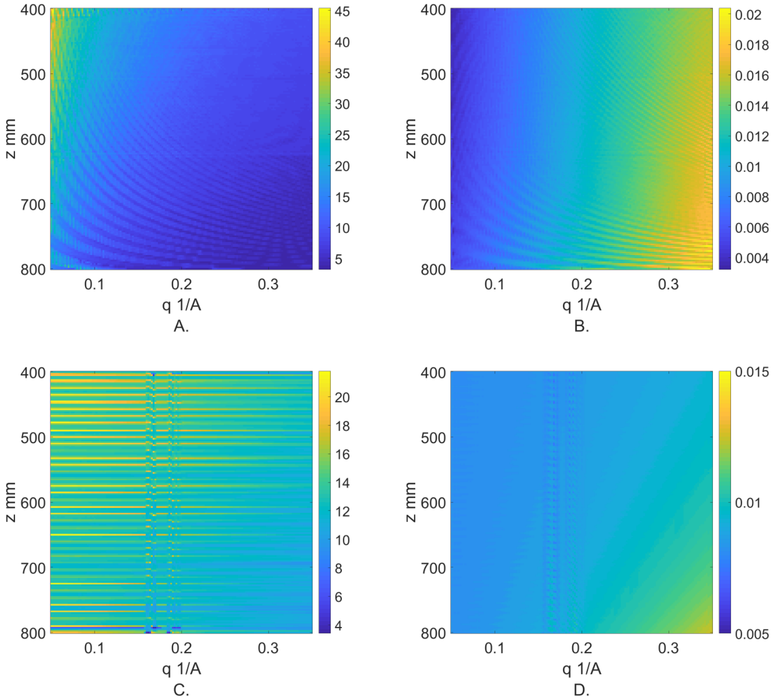

Figure 4. System resolution determined by the Gramian approach: A.) Coded aperture spatial resolution (mm) B.) Coded aperture momementum transfer resolution ($1/\mathring{A}$) C.) DT spatial resolution (mm) D.) DT momentum transfer resolution ($1/\mathring{A}$)

repeated for all rows in the Gramian. Here, we find reasonable agreement between the theoretic relations and the predictions derived from our method outlined above as will be discussed further. Utilizing this approach, we then compute the spatial and momentum transfer resolutions for a 1D DT and CA-XRDT system, and in Figure 4, we display these results for the two systems we have deemed “matched”. Again, the precise resolution depends on the combination of both z and q, and direct comparison between the two architectures is slightly challenging given that the scaling for each system is not identical. As would be expected, we observe that the spatial resolution in the CA-XRDT system worsens as we get further away from the coded aperture (i.e. moving towards the lower z values) and for lower q values since one obtains smaller and fewer projected code features at the detector.

To better interpret the data, we then calculate the average resolution for each system and display the average spatial resolution across q and the average momentum transfer resolution across z in Figure 5. Here, we also overlay averaged predictions derived from the analytic relations presented in Section 2 of this work, and overall, there is reasonable agreement between the two. The theoretic relations, however, tend to slightly underestimate the resolutions for both curves, relative to that predicted by the Gramian, and furthermore, the two methods seem to suggest a different scaling for the average spatial resolution of the DT system. We also highlight that the DT average spatial resolution derived from the Gramian oscillates rapidly with z between an upper and lower bound, and we find that this is due to overlaps in the projected field of view for the detector pixels. At locations in z where two or more detector pixels receive the signal, the spatial resolution is improved and as a note, this suggests that one can actually open up the collimation more that naively expected and still achieve good resolution via model-based reconstruction. This feature is also observable in the unaveraged spatial resolution displayed in Figure 4C. Furthermore, in both the unaveraged DT resolutions, 4C. and D., one also observes spikes in the resolution for both $q \approx 0.16$ and $0.18\ 1/\mathring{A}$, and these q-values interestingly correspond to the brightest characteristic peaks in the simulated tube spectrum (when converted to q space). Overall, we find these CA-XRDT and DT systems to be well-matched in terms of average resolution, and we highlight that both sets of resolutions largely remain the same in the transition from a 1D to 2D geometry, given that we do not further alter the feature sizes on (or locations of) the detector or optical components.

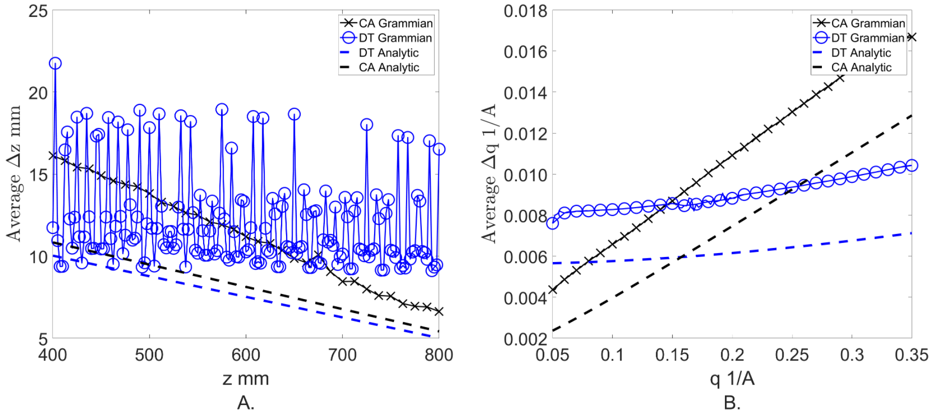

Figure 5. Average resolution for the matched 1D CA-XRDT and DT system: A) Average spatial resolution across q and B) average momentum transfer resolution across z. Solid lines indicate the Gramian prediction and dashed lines correspond to the theoretical prediction discussed in Section 2.

4. PERFORMANCE ANALYSIS

With our matched DT and CA-XRDT systems, we next simulate the detector measurement for each in response to the same object vector. We then compute a maximum likelihood reconstruction on both detector measurements in order to get back estimates of the starting object vector, and this step serves to both demulitplex the signal (as is necessary for CA-XRDT) and to sharpen the estimate. The reconstructed estimate of the object for each system is then compared against the original, ground truth object, and we utilize two different metrics to quantify the spatial and spectral accuracy. The remainder of this section will be dedicated to elaborating on this approach, and in Section 4.1, we present further discussion into the subtleties and choices made in this study for the object vectors probed, the trade-space analyzed, and the dimensionalities of the CA-XRDT and DT systems modeled. In Section 4.2, we discuss the specific reconstruction algorithm utilized and give context on alternate (and perhaps better) options that may be used in the future, and in Section 4.3, we elaborate on the metrics and rationale therein for comparing the quality of the reconstructed object vector estimates.

4.1 Simulation parameters

The focus of this work is in understanding how the performance varies when imaging a single-composition object as a function of the number of incident photons, here defined by the product of the integration time and the tube current of the simulated measurement (given in units of mAs), and the width of the target object along the pencil beam. Throughout this work, we utilize a Poisson noise model for the measurement, and we highlight that defining performance in terms of realistic mAs settings for the tungsten tube, as opposed to in terms of SNR, is advantageous since the range of SNR values characterizing the detector measurement will be object dependent. Focusing first on the aspect of signal strength, creating an interpretation for our results that is physical and meaningful requires that we first ensure that our diffraction-detection model predicts a number of scattered photons per mAs which is consistent to that observed experimentally. In validating this, we assert that our treatment of the physics and geometry is correct and that any discrepancy between the experimental and simulated values for the number of incident photons resides in an incorrect absolute amplitude of the simulated tungsten spectrum (see Section 3.2), defined in this work for a given focal spot size in terms of number of photons/$[\text{mAs} \cdot \text{KeV}]$. In order to identify the scale-correction factor to the simulated tube amplitude, we utilize an experimental, test bed pencil-beam XRD system, described in greater detail in past work,[4] to obtain a 2D, multi-energy diffraction measurement for an Aluminum powder vial. The data is collected utilizing the same tungsten tube for which we are investigating in the simulation and an acquisition is obtained on the system, operating continuously at a tube potential of 160 kV and 67.5 mAs, in combination with photon-counting (Multix ME-100) detectors. We find that the simulated measurement agrees well with the experimental measurement after the tube spectrum is scaled appropriately to the correct absolute intensity value, and throughout this work, we utilize the same scale factor to the tube spectrum in order to tune the simulated signal strength in terms of a mAs value.

In addition to tuning the mAs, the second parameter of interest for this study is the spatial extent of the objects along the pencil beam, and the motivation for probing the influence of this lies in our expectation that the CA-XRDT system will have more difficulty for longer objects. Specifically, as we increase the set of continuous object voxels that are illuminated, there will be more overlapping signal at the detector when no collimation is present. While it is obvious that this makes for a more challenging reconstruction, a quantitative estimate of the physical extent which causes diminishing performance and a breakdown in the CA-XRDT reconstruction is not well known. In terms of the specific objects that we simulate in this study, we choose from a set of over 400 materials for which we have experimentally measured the form factor of using a Bruker D2 diffractometer.[15] We note that the Aluminum powder form factor that was used in the simulation displayed in Figure **??** and discussed earlier in this section was obtained from this set. Furthermore, in utilizing the form factors as a probability of scatter, we again normalize the $f(q)$ for a given z voxel such that the area under the curve is one and then scale the resultant form factor by the energy-dependent Rayleigh scattering cross-section and density. Throughout this work, we make the approximation that the coherent scatter cross-sections for all materials are the same, and we compute the calculations utilizing the cross-sections for H_2O as obtained again from the NIST XCOM database.[16] While this is not completely true, it is a fair approximation as the differences in the probability of scatter across materials are relatively small (generally a few percentage points). Furthermore, while the density of the materials can vary significantly, we note that our final results will be averaged over many materials and we expect that such variations will be averaged out in the end.

Although we have a large set of form factors from which to choose from for this study, we emphasize that the particular choice of materials used as the objects is, in fact, rather important to consider in order to get generalizable results. Specifically, certain structures in the form factors prove easier to reconstruct and image than others, and it is important not to bias the performance analysis by virtue of the selection of the object set. One can further consider this by recognizing that, for both system architectures, a sharp, single peak form factor will have all the scattered photons concentrated to a smaller spatial density at the detector as compared to the scatter distribution from a broad form factor, and given that we have included Poisson noise, this then implies that we are here imaging with a better SNR for the features of interest. Furthermore, considering the consequences of structural differences in the form factors is also important because it inherently encapsulates the reconstruction challenges for a single-composition extended object in a CA-XRDT system: a broad form factor scattering from multiple locations along the path of the beam presents significant overlap at the detector due to the $z-q$ ambiguity in Bragg's law. Said in an alternate way, a particular z location can scatter to the same detector pixel as another location via a scattered photon with a different momentum transfer, and the total number of object voxels to disambiguate with the coded aperture here scales non-linearly with the spread of the form factor.

Recognizing that these two considerations are thus important, and summarizing the sharp and broad form factors as low and high complexity spectra, respectively, we note that choosing objects of only low complexity would suggest far better performance for both systems, especially the CA-XRDT system, than would result in a real world application. Alternatively, only imaging high complexity objects like water and other liquids would make it difficult to disambiguate if a breakdown was due to object extent or insufficient SNR. While focusing on just one extreme would be interesting to test in a task-specific study, in this work we choose an object set by sampling evenly throughout the range of spectra complexities and repeat the analysis for each to obtain a more generalized result. In order to do this, we then need to assign a quantitative value for the imaging complexity of a form factor in this context so that we can then rank and sample the spread. We choose to assert a definition of complexity for this work that is independent of system architecture and encapsulates the feature dynamics described above. For each form factor, we convolve the spectrum with a rectangular pulse 0.008 $1/\mathring{A}$ wide, normalize by the maximum value, and then take the total area under the curve. The role of the convolution is to take into account approximate q-resolution of both systems since many sharp peaks close together in q ultimately appear to the system as a single peak, broad spectrum. In Figure 6A., we show all form factors in the data set sorted by this area from least to greatest (and thus from lowest complexity to highest complexity). In plot B. of the same figure, we have isolated examples of low, mid, and high complexity form factors based on this definition, and we find the ranked descriptions consistent to our intended characterization. Furthermore, while far less influential than the prior consideration, we also note that spatial and spectral resolutions for each system have some dependence on the object's location in z. To further account for this range and to prevent additional bias, we seed each object considered at a random location in z, subject to the constraint that the object remains within the simulated object space even when extending the object's width along the pencil beam to the maximum distance considered here.

Lastly, we conclude our review of the simulation parameters by describing the precise detection geometries simulated in this work. Here, we consider a pencil beam setup with the z axis defined parallel to the primary X-ray beam and with the tube focal spot at $z = 0$ mm. The object is then placed (and fully contained) between $z = 400$ to 800 mm and the detector is placed at $z = 1200$ mm. When the coded aperture is simulated, it is placed directly after the object cut-off at $z = 815$ mm and the collimation for the DT system is considered attached to the detector plane. Here, we consider both 1D and 2D energy sensitive detectors, and for the coded aperture design, we utilize a mask with a 1D sinusoidal pattern and a 2D random binary pattern, respectively. Similarly, the DT collimator consists of a single angle transmission grid, and we note that the properties of the 1D and 2D collimators are the same but with the 2D version allowing the transmission of rings of scatters focused about individual object voxels. Furthermore, we highlight that in transitioning from a 1D to 2D CA-XRDT architecture, a new forward matrix must be generated since the details of the coding (and thus the invertibility of the forward matrix) changes; however, for the DT architecture, a new forward matrix is not necessary since the change can instead be effectively described as an increase in signal for the 1D measurement since all detector pixels at a given radial distance from the primary beam obtain the same measurement. This remains valid even after noise is added due to the additive property of the Poisson model.

We highlight that we are able to achieve a matched resolution between the CA-XRDT and DT systems for all scenarios studied here by modifying only the coded aperture feature size and the DT collimation angle and

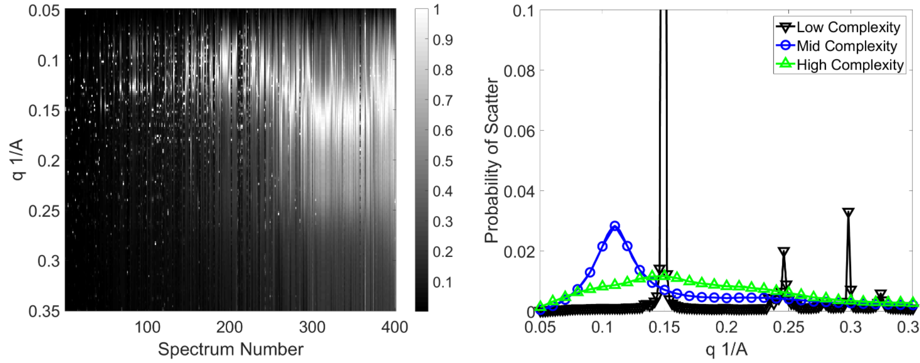

A. B.

Figure 6. Form factors used for the simulated objects. The full data set is displayed in A) and is sorted from lowest complexity (left) to highest complexity (right). B) We isolate and plot the $f(q)$ for a low, mid, and high complexity spectra. The y-axis is cropped to allow better view of the high complexity shape.

angular field of view. Specifically, we are able to keep the aformentioned geometry (detector and object locations) and key detector properties (the pixel sizes and energy resolution) the same throughout this work. As a consequence of this, we are able to probe two different approaches for the comparative study: we consider the detection performance for "matched hardware", where the same detector is used and the only difference between the two systems is the inclusion of a coded aperture or collimation grid in between the object and detector, and we also consider the case of "matched dimensionality", where the total number of measurements (across both space and energy) is the same for the two systems.

In Table 1, we summarize the details of the detection area and energy channels avaialble to the CA-XRDT and DT architectures for each case. We highlight that in the 1D "matched hardware" scenario, both architectures are provided with a 16 cm long, linear detector; however, the DT architecture here has a direct mapping between pixels and object voxels (with single angle collimation) utilizing a length of only 2.8 cm along the 1D detector. All other pixels outside this range receive no signal and are unused, and this is a consequence of the imaging approach itself, which allows little spatial extent to reduce multiplexing and instead images through energy. Alternatively, the coded aperture implementation instead allows for acceptance of a wider range of scatter angles, and imaging through all z-q pairs in every energy channel in fact requires a linear detector longer than that used here; Instead, we find that it is sufficient to enforce that all z-q pairs are imaged, albeit in only some energy channels and not others, and the CA-XRDT measurement utilizes the full length of the detector array. The "matched dimensionality" case instead requires that the ≈4300 useful measurements in the aforementioned 1D DT detection and the ≈29000 useful measurements in the CA detection be better equalized. We consider the number of effective pixels–meaning pixels that actually receive signal at the detector–for the DT case to be already minimized, and in order to then reduce the CA-XRDT detection dimensionality, we can utilize only a subset of the energy bins (which also then reduces the spatial extent of scatter at the detector). In this case, which primarily serves to be instructive and exemplary of the type of comparisons that can be made, we emphasize that this CA-XRDT implementation is far from optimized, particularly given that we are imparting spatial and not spectral coded modulations to the diffraction.

We also consider the case of a detector with a two-dimensional array of pixels, where we probe another "matched dimensionality" comparison but with the CA-XRDT system better conditioned. Here, we instead consider a single energy channel for the CA-XRDT measurement and focus on capturing the full spatial scatter on the detector. For the DT architecture, all 111 energy channels of the now 2D detector are again required

Table 1. Summary of detector properties and optical components across the three simulation scenarios analyzed in this work. The 1D area is formed by a line of 0.75 mm square pixels. In the 2D case, we assume a circular shaped detector with a hole in the center.

Scenario	**Detector Area** cm^2		**Energy Channels** KeV		CA Type	Collim. Type
	CA	DT	CA	DT		
1D Matched Dimension.	5.94	2.80	40.3-80.3 (40 bins)	17.3-127.3 (111 bins)	0.5 mm sinusoidal binary	4°±0.025° line grid
1D Matched Hardware	16	16	17.3-127.3 (111 bins)	17.3-127.3 (111 bins)	0.5 mm sinusoidal binary	4°±0.025° line grid
2D Matched Dimension.	433.46	5.27	59 (1 bin)	17.3-127.3 (111 bins)	0.5 mm 50% random binary	4°±0.025° annulus grid

in order to image the full range of q at an appropriate sampling; however, this then implies that there is an insufficient number of remaining measurements to then capture the full rings of scatter as transmitted by the 2D collimator. In this case, we then settle with capturing only a subset of the full scatter annulus, 1/15th of each ring specifically, such that both systems again have the same number of total spatial plus spectral measurements. In the 1D matched dimensionality case, the CA-dimensionality was reduced but for the 2D case, we here reduce the DT-dimensionality. For both systems, the transition from a 1D to 2D detector space, even with the constraint on dimensionality, still presents an improvement to the signal levels at the detector and serves as an example of how the performance changes as a result. The results from all three scenarios outlined here – the 1D "matched hardware" case, the 1D "matched dimensionality" case, and the 2D "matched dimensionality" case – are presented and discussed in Section 5.

4.2 Object reconstruction

After simulated measurements are obtained from the systems described above, it is then the goal of X-ray tomographic imaging to deduce the object vector, i.e. the object location and its characteristic form factor, which uniquely could have produced the measured pattern. Specifically, in terms of the forward matrix approach displayed in Equation 8, one must solve the inverse imaging problem where $\mathbf{g}$ is the measurement and $\mathbf{H}$ is assumed to be both known and well matched to the system in question. The challenge generally, however, is that $\mathbf{H}$ is not directly invertible, and as a result, image reconstruction algorithms (most commonly iterative approaches) must be utilized in order to derive an estimate to the object vector, here referred to as $\hat{\mathbf{f}}$. In this work, we utilize a maximum-likelihood expectation-maximization (MLEM) approach and greater details of our particular implementation has been discussed by MacCabe et al.[3] For this work, we choose to terminate the algorithm after 600 iterations, which we find to be sufficient. We emphasize that the performance results depend greatly on the maximization algorithm utilized, and we have chosen to use this simple MLEM approach not because it is the best or most optimized solution, but because it serves as a "baseline" algorithm which is computationally quick, well-known, and has a published history of implementation to similar image reconstruction problems for other X-ray tomography modalities.[17–20] Specifically, in our approach, we have assumed no a priori information about the nature and properties of the object space, and doing so likely underestimates the tomographic potential of a system, particularly for the CA-XRDT architecture. In reality, one can implement regularization and alter the penalty function based on constraints for object smoothness, probabilistic object distributions, or simply, the total variation in the space and doing so will allow one to better obtain an object vector estimate from a set of multiple possible solutions when the inverse problem is particularly ill-posed.[21]

4.3 Performance metrics

In this work, imaging performance is analyzed for 21 materials randomly placed within the object space and for various combinations of tube mAs and object widths. For each case, we compare the final reconstructed estimate of the object vector, $\hat{\mathbf{f}}$, against the ground truth vector, $\mathbf{f}$, and quantify the error in both spatial localization and form factor characterization with an error metric defined as,

$$\text{Error} = \frac{\sum \left|\hat{\mathbf{f}} - \mathbf{f}\right|}{\sum \mathbf{f}}, \tag{10}$$

where $|\cdot|$ denotes the absolute value. Here, we have chosen to equally penalize spatial error and form factor error in the predicted vector, and we note that this definition of error also enforces that the predictions of $f(q)$ preserve the absolute intensities of features and not just the shape. Furthermore, the normalization in the metric is important and this scaling allows the interpretation of the error quantity to remain the same even as the object increases in size. To complement this metric, we also compute the average, squared Pearson's linear correlation coefficient between the reconstructed and ground truth form factors (examining only the object voxels in z where the object is known to be located). This metric is independent of the relative scaling between the two curves and only examines the similarity in shape and structure. Generally, we have found in this work that, for CA-XRDT, the accuracy of the predicted form factor is closely coupled with the spatial accuracy and that it would a sufficient approximation to validate both by validation of one or the other. This fact, however, is not true for DT where the system inherently provides little ambiguity to localization in z independent to its ability to predict $f(q)$, and for this reason, both metrics outlined here are useful in conjunction for a comparative analysis between the two systems.

5. RESULTS

First, considering four tube mAs parameters spanning the full range considered in this work, we compute the error metric as a function of object width for 21 materials selected to span the range of form factor complexities. The mean performance and standard deviation for a given object width and mAs initialization across the 21 objects is then determined and the resulting curves are displayed in the left column of Figure 7. Here, we have conducted this analysis for the three detection scenarios outlined at the end of 4.1, i.e. 1D or 2D detectors with a matched hardware or matchsectioned dimensionality comparison between the two architectures, and in interpretating the plots, we highlight that a lower error value indicates better performance. In addition, we isolate an object of mid-complexity from the examined set and compute the Pearson's correlation coefficient for the predicted $f(q)$ against the ground truth in the object voxels where the object is known to be located. The corresponding mean correlations are shown in the right column of the figure. Again, these serve to complement the error metric and provide intuition for an approximate correspondence between error and potential form factor classification performance (if a correlation based classifier is used).

In all three design studies and for all four mAs values shown, we note that the DT system has large error when imaging objects that have a width along the beam shorter than the average z resolution of the system, which is approximately 10 to 20 mm (as shown in Figure 5). This is consistent with expectation given that the scatter from thin objects gets associated and blurred to multiple object voxels by virtue of the field of view for the detector pixels. In addition, we also highlight that the standard deviation is largest for the these thin objects, and this can be understood in terms of the large variation in the DT average z resolution–if an object voxel is located where the field of view from multiple pixels overlap, finer resolution and localization is possible. Alternatively, for objects wider than the average resolution, we observe that the performance for the DT system stabilizes and is approximately independent to the object width, as it should be given that the collimation prevents multiplexing. In contrast, we highlight that the CA-XRDT system error is minimized for small objects, and performance generally gets worse with increasing object width until the error eventually converges to an upper limit. Here, we can observe the breakdown of CA-XRDT due to multiplexing, regardless of mAs; however, in comparing the 1D to 2D errors (or even the 1D matched hardware to the 1D matched dimensionality case), we note that this challenge can be entirely overcome (or significantly improved) by allowing a greater degree of spatial coding. Furthermore, highlighting plots B, and D., we note that the DT architecture generally obtains a greater percent improvement to the spectral correlation per increase in mAs than for CA-XRDT, and this stems from the fact that the primary challenge for a DT system to overcome is SNR. For CA-XRDT, improving SNR

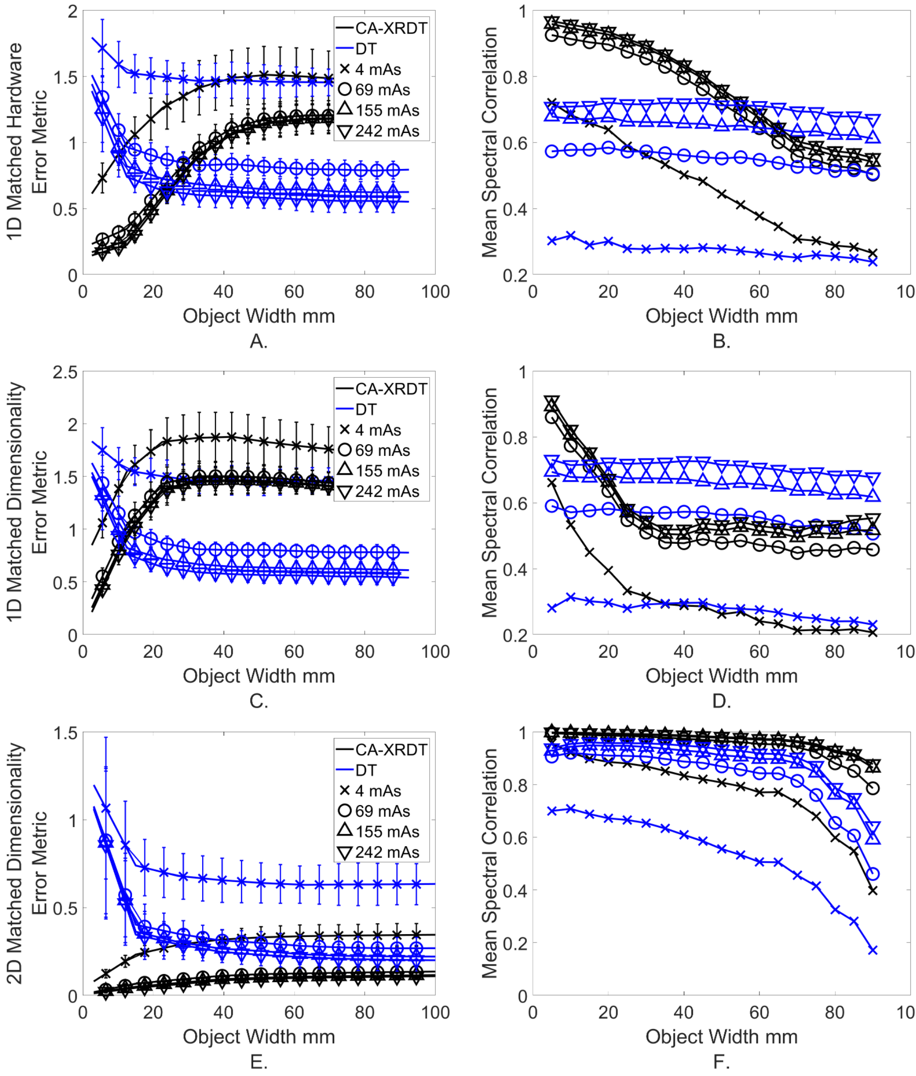

Figure 7. (Left Column) Mean error for reconstructed object vectors (600 iterations) relative to the ground truth for select mAs values. (Right Column) The corresponding, average linear Pearson's correlation coefficient evaluated for the mid complexity object. Top row displays the 1D "matched hardware" case, middle row displays the 1D "matched dimensionality" case, and bottom row displays the 2D "matched dimensionality" case.

quickly presents diminishing returns since the primary challenge which should instead be addressed is multiplexing by virtue of object width.

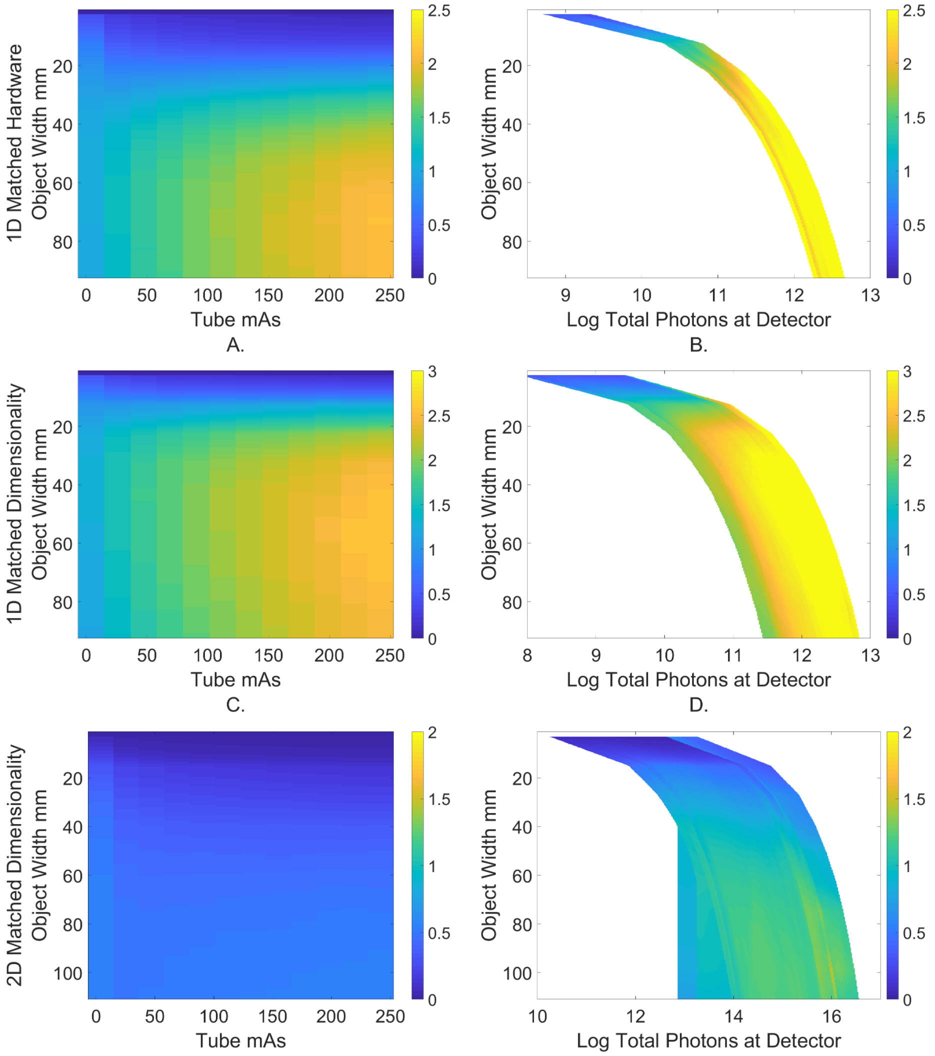

A. B.

C. D.

E. F.

Figure 8. (Left Column) Ratio of the mean CA error to the mean DT error for a given object width and tube mAs (Right Column) Ratio of the CA error to the mean DT error for a given object width when the total number number of photons measured at the detector is the same.

We highlight that the important take-away from these plots is the intersection between the CA-XRDT and DT performance. For all SNR values in the 1D case, we observe that the coded aperture architecture outperforms the DT system (subject to the same SNR) when the object width is small but then find that the DT system gains the advantage for extended objects. When the coded aperture architecture is optimized, however, like in the 2D case shown in plot E. and D., we note that the CA-XRDT system outperforms the DT system (at the same SNR) for all the four mAs values. As an extension of this, we compute the same error calculation as done above, but now for 12 different mAs values. We then take the ratio of the mean CA error to the mean DT error for a given object width and mAs initialization and display the distribution for the three design studies in the left column of Figure 8. To aid in interpretation, we highlight that values less than one indicate that the CA-XRDT system outperforms the DT system while values greater than one suggest the converse. Here, we observe more generally that there exists regions, for the 1D case, where one architecture is better suited and conditioned for tomography than the other, and for this particular, 2D example where total system dimensionality is held constant, we observe a significant advantage to the CA-XRDT implementation throughout the entire operation space considered. Again, this is but one design example and a different comparative study– likely along the lines of each system individually optimized–may be of practical interest.

While we observe that the CA-XRDT implementation measures more photons (which allows it to perform better than DT at low mAs settings), we can also determine from this data which architecture obtains more information per photon arriving at the detector. Here, we take the mean CA-XRDT error and mean DT error for a given object width and compute the ratio when both systems have the same number of measured photons at the detector. Specifically, this overlap in total detected photons occurs when comparing the CA-XRDT system at low mAs settings against the DT system at high mAs settings, and the value of this ratio allows one to interpret the relative information content per photon. The results of this calculation are shown in the right column of Figure 8. In general, we find that for all object widths greater than the DT system resolution, the DT system contains more information per photon, which is consistent with expectations and the general motivation behind the DT design. We emphasize, however, that the challenge in most practical scenarios lies not in the information content but in obtaining enough photons to begin with.

6. CONCLUSIONS

In summary, we have presented in this work a generalizable, simulation-based approach to compare the relative performance of a CA-XRDT and DT system for arbitrary object configurations and realistic SNR conditions. This methodology can be adapted to address task-specific imaging scenarios and system design constraints; however, we analyzed here the two architectures in the context of a matched resolution, "fair" comparison. We have presented analytic relations to define the spatial and momentum transfer resolutions for each system alongside a numerical, model-based method, and we find the prediction from both methods to be in good agreement. From this apples-to-apples study, we observe intersections and overlaps in the relative performance, and conclude that there are particular regimes in which one system outperforms the other by virtue of the fundamental system architecture. In the future, a continuation of this study can be performed, replacing the image reconstruction procedure in favor of an information theoretic analysis on the simulated measurements themselves. In addition, we can consider other comparison scenarios such as the case of CA-XRDT and DT systems with matched costs as well as transition from quantifying the object estimate fidelity to ranking the classification performance of these systems.

ACKNOWLEDGMENTS

This material is based upon work supported by the U.S. Department of Homeland Security, Science and Technology Directorate, Office of University Programs, under Grant Award 2013-ST-061-ED0001. The views and conclusions contained in this document are those of the authors and should not be interpreted as necessarily representing the official policies, either expressed or implied, of the U.S. Department of Homeland Security.

REFERENCES

[1] J.Greenberg and K.Iniewski, [*X-Ray Diffraction Imaging: Technology and Applications*], Devices, Circuits, and Systems, Taylor & Francis Group (2018).

[2] G.Harding, H.Fleckenstein, D.Kosciesza, S.Olesinski, H.Strecker, T.Theedt, and G.Zienert, "X-ray diffraction imaging with the multiple inverse fan beam topology: Principles, performance and potential for security screening," *Applied Radiation and Isotopes* (2012).

[3] K.MacCabe, K.Krishnamurthy, A.Chawla, D.Marks, E.Samei, and D.Brady, "Pencil beam coded aperture x-ray scatter imaging," *Optics Express* (2012).

[4] J.A.Greenberg, C.MacGibbon, D.S.Hazineh, B.Keohane, and S.Wolter, "The role of texturing in x-ray diffraction tomography," in [*Anomaly Detection and Imaging with X-Rays (ADIX) III*],

[5] V.Sridhar, S.J.Kisner, S.Skatter, and C.A.Bouman, "Model-based reconstruction for x-ray diffraction imaging," in [*Anomaly Detection and Imaging with X-Rays (ADIX)*],

[6] S.Skatter, S.Fritsch, and J.P.Schlomka, "Detecting liquid threats with x-ray diffraction imaging (xdi) using a hybrid approach to navigate trade-offs between photon count statistics and spatial resolution," in [*Anomaly Detection and Imaging with X-Rays (ADIX)*],

[7] M.J.E.Golay, "Multi-slit spectrometry*," *J. Opt. Soc. Am.* (1949).

[8] M.E.Gehm and J.Kinast, "Adaptive spectroscopy: towards adaptive spectral imaging," in [*Anomaly Detection and Imaging with X-Rays (ADIX)*],

[9] M.Hassan, J.A.Greenberg, I.Odinaka, and D.J.Brady, "Snapshot fan beam coded aperture coherent scatter tomography," *Optics Express* (2016).

[10] J.A.Greenberg, K.Krishnamurthy, and D.Brady, "Snapshot molecular imaging using coded energy-sensitive detection," *Optics Express* (2013).

[11] J.A.Greenberg, K.Krishnamurthy, M.Lakshmanan, K.MacCabe, and S.Wolter, "Coding and sampling for compressive x-ray diffraction tomography," in [*Proceedings of SPIE*],

[12] G.G.Poludniowski and P.M.Evans, "Calculation of x-ray spectra emerging from an x-ray tube part i. electron penetration characteristics in x-ray targets," *Med. Phys.* (2007).

[13] G.G.Poludniowski, "Calculation of x-ray spectra emerging from an x-ray tube part ii. x-ray production and filtration in x-ray targets," *Med. Phys.* (2007).

[14] Poludniowski.et.al., G., "Spekcalc: A program to calculate photon spectra from tungsten anode x-ray tubes," *Phys. Med. Biol.* (2009).

[15] S.D.Wolter and J.A.Greenberg, "Spectral feature variation in x-ray diffraction imaging systems," in [*Anomaly Detection and Imaging with X-Rays (ADIX)*],

[16] M.J.Berger.et.al., "Xcom: Photon cross section database (version 1.5)," [online] Available: http://physics.nist.gov/xcom.

[17] A.J.Rockmore and A.Mocavski, "A maximum likelihood approach to emission image reconstruction from projections," *IEEE Trans. Nucl. Sci.* (1976).

[18] L.A.Sheep and Y.Vardi, "Maximum likelihood reconstruction in positron emission tomography," *IEEE Trans. Med. Imag.* (1982).

[19] K.Lange and R.Carson, "Em reconstruction algorithms for emission and transmission tomography," *J. Comp. Ass. Tomogr.* (1984).

[20] J.M.Ollinger, "Maximum-likelihood reconstruction in transmission images in emission computed tomography via the em algorithm," *IEEE Trans. Med. Imag.* (1994).

[21] [*Handbook of Research on Emerging Perspectives in Intelligent Pattern Recogniztion, Analysis, and Imaging Processing*], ch. Total Variation Applications in Computer Vision, IGI Publishing (2016).